THE LEADING ARM, RINGED SPIRAL GALAXY NGC 4622: A DIAGNOSTIC CASE OF A RETROGRADE TIDAL ENCOUNTER

R. BUTA,[1] D. A. CROCKER,[1] AND G. G. BYRD
Department of Physics and Astronomy, University of Alabama, Box 870324, Tuscaloosa, Alabama 35487
Received 11 December 1991; revised 22 January 1992

ABSTRACT

The southern galaxy NGC 4622 is a rare example of a spiral with two sets of spiral arms winding in *opposite* senses: A single inner arm which opens counterclockwise, and two outer arms which open clockwise. The two sets of arms are linked by a nearly circular, off-centered inner ring of high contrast, and the presence of the two opposing senses means that NGC 4622 has at least one *leading* spiral arm, a phenomenon that up until now has never been firmly established in *any* galaxy. In this paper, we describe some of the basic morphologic and photometric properties of this galaxy, which has recently been suggested to have experienced a retrograde tidal encounter. Of the three observed arms, the inner arm is the prime suspect for the leading sense, based on published *n*-body models. We establish with *BVI* surface photometry that this arm is present in the stellar disk component and is not an artifact of dust absorption. The suspected leading arm begins $\approx$3 kpc from the center and winds more than 360° to a radius of $\approx$4.4 kpc. The winding is logarithmic in projection with a pitch angle of only 4°. A substantial portion of the inner ring may be made of the leading arm. A large variation in $B-I$ color index around the ring is also found. At the average radius of the ring, the phase of the 1θ Fourier component in B is shifted $\approx$40° in the direction of rotation relative to that in I. The shift is consistent with the hypothesis that part of the ring is a one-armed density wave turning opposite the disk rotation at $\approx$1.4 times the orbital speed. The galaxy may be the most definite case to date demonstrating this density wave effect because of the large difference between the leading arm pattern rate and the orbital rate. The perturbing companion has not yet been identified. We suspect that a small galaxy 1'.85 east, of unknown redshift, may be the most promising to explain not only the leading arm, but also the two trailing outer arms.

1. INTRODUCTION

Kinematic studies of galaxies where the apparent dust distribution allows us to unambiguously distinguish the near side of the disk have indicated that spiral arms generally trail the direction of rotation (de Vaucouleurs 1958, and references therein). However, it is now well known that retrograde tidal encounters between neighboring galaxies can generate a *leading arm*, particularly in the region of the +1:1 resonance of the disk material's orbital and epicyclic motion with the angular velocity of the companion. The forcing can be periodic, as in the case of a companion on circular orbit (Athanassoula 1978), or short term, as in an unbound encounter (Noguchi & Ishibashi 1986, hereafter referred to as NI86; Thomasson *et al.* 1989, hereafter referred to as T89; Thomasson 1990; Athanassoula 1992). A leading arm forms in such encounters if the halo-to-disk mass ratio within the disk radius is large (T89). Any potentially genuine case of a leading arm is, then, of great interest because even though galaxies with heavy haloes are thought to be very common, known cases of leading arms are extremely rare. It would also provide an important example to compare with models of tidally generated spiral structure.

The nearly face-on southern spiral galaxy NGC 4622 (= ESO 322 – 57, MCG – 7 – 26 – 31, AM 1239 – 402, Fa33, PGC 42701) provides one of the most convincing cases of a leading spiral arm in *any* galaxy. The feature was first recognized by Byrd *et al.* (1989, hereafter referred to as B89) on a commercially available, blue-light NOAO photograph as being located inside an off-centered inner ring. The galaxy, which has several nearby disturbed-looking companions, also shows two outer spiral arms beginning at the ring which wind outward in the opposite sense to the inner arm. NGC 4622, therefore, has to have either one leading arm inside the ring with the two outside the ring being normal trailing arms, or the reverse. There are good reasons, both theoretical and observational, to believe that the inner arm is the leading one, therefore, we shall refer to it as such throughout this paper. The ring and inner arm bear a striking resemblance to the T89 and NI86 simulations. Since any further evaluation of these simulations required more detailed data than on the photograph available to B89, follow-up work on this galaxy was critically needed. In particular, we are concerned about whether the apparent leading arm might be an artifact of dust in the galaxy or is truly present in the stellar disk component.

Our main purpose with this paper is to establish the reality of the leading arm using multicolor CCD surface photometry. With such photometry, we can deduce the stellar population of the arm compared to its surroundings, and use Fourier analysis and photometric decomposition to enhance its visibility. The observations are discussed in Sec. 2, and the morphology and color distribution in Sec. 3. Surface photometry is presented in Secs. 4 and 5, and techniques for enhancing the leading arm are presented in Sec. 6. The data are discussed in Sec. 7. Conclusions are in Sec. 8.

2. OBSERVATIONS

The photometric observations were obtained using the No. 3 TI CCD on the 1.5 m telescope of Cerro Tololo Inter-American Observatory in 1990 February. A 2×2 on-chip binning was used, giving pixels 0".54 by 0".54 in size. The field

[1] Visiting Astronomer, Cerro Tololo Inter-American Observatory, National Optical Astronomy Observatories, which is operated by the Association of Universities for Research in Astronomy, Inc. (AURA), under cooperative agreement with the National Science Foundation.

 0004-6256/92/051526-10$00.90

of view was 3'.6 square. Filters which match the Johnson *BV* and Cousins *I* systems were used, and the average airmass was 1.023. Each exposure was preflashed, therefore, a large number of bias frames was combined to enable subtraction of this "fat zeroing." Flatfields consisted of combined dome and sky flats. Fringes were observed in the *I* band at an amplitude of 1%–2% of the night sky, and were removed by imaging a blank sky field chosen from an unpublished list by Graham and Seitzer. Since no single exposure was longer than 300 s, no dark frames were needed. All processing of the calibration frames and calibration of the images was done with standard routines in IRAF.[2]

Zero points and transformations to the standard *BVI* systems were obtained from both aperture photometry on the galaxy itself and from CCD observations of standard star fields. The photoelectric aperture photometry was taken from Buta & Crocker (1992), who measured the galaxy with four apertures ranging from 20″ to 116″ in diameter. Transformation of this photometry to the Johnson *UBV* and Cousins *RI* systems was accomplished with *E*-region standards (Menzies *et al.* 1980). The standard stars for the CCD photometry included only fields from Graham (1982) and Landolt (1983), and thus are largely independent of the photoelectric calibrations. As a check on the CCD calibration, we simulated aperture photometry on the CCD images within the four apertures and applied the standard star extinction and transformation coefficients and zero points. The results were compared with the photoelectric photometry, and showed average residuals less than $\pm$ 0.03 mag in all magnitudes and colors. We feel that the photoelectric photometry is more reliable for zero points, therefore, we used the CCD standard stars only for extinction and transformation coefficients.

3. MORPHOLOGY AND CLUSTER MEMBERSHIP

NGC 4622 is a spiral of type SA(r)ab. Our *B*-band image is displayed in the upper-left panel of Fig. 1 [Plate 88]. The morphology is dominated by a large, round bulge and two high contrast outer arms which appear to terminate in a nearly circular inner ring. The suspected leading arm is located inside of this ring and is prominent west and northwest of the bulge (see schematic in Fig. 2). The ring itself is miscentered on the bright nucleus and may be partly made of the leading arm. The two bright outer arms do not break from the ring at diametrically opposite points, nor do they wind symmetrically.

To demonstrate that the leading arm is not an artifact of dust, we illustrate in the upper-right panel of Fig. 1 a $B-I$ color index map. The gray scale is such that the darkest features have $B-I \approx 1.75$ and the lightest features have $B-I \approx 2.75$. This map shows no evidence for dust lanes inside the inner ring, even with the large wavelength difference. Also, there is no clear color differentiation associated with the leading arm, except where it appears to merge with the ring due north of the nucleus. The east half of the inner ring is barely visible in the color map, while the west half is very prominently blue [see Fig. 11(d), Sec. 6, for a quantitative display of this color variation]. This is very unusual compared to most "normal" rings, which are usually symmetric blue enhancements (see, e.g., Buta 1991, and references therein). The two outer arms are much clearer enhancements of bluer colors than the ring. These aspects are quantified further in Sec. 5.

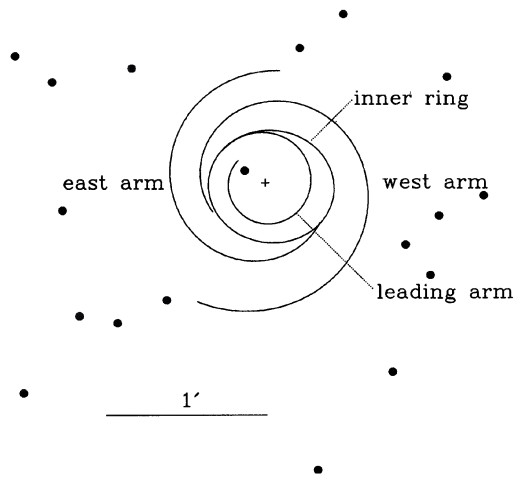

FIG. 2. Schematic of NGC 4622 with major features labeled. Plus symbol indicates the nucleus, and filled circles indicate some of the brighter foreground stars.

Shu (1982) presents NGC 4622 as an example of a classic two-armed spiral. Using an excellent, commercially available, NOAO 4 m CTIO photograph for an illustration, he notes that "strong dust lanes can be readily seen on the inside edges of the optical arms." However, it is noteworthy that our $B-I$ map reveals no evidence for such lanes at the resolution of our images. This shows the importance of obtaining multicolor images to better establish the existence of dust lanes, which are important in density wave theory. It was the illustration in Shu's book that, in 1987, left Byrd with a strong suspicion that there was a leading arm in the inner parts of NGC 4622 (B89).

NGC 4622 is a member of the Centaurus Cluster (see Region IV of de Vaucouleurs 1956), and has two nearby companions of comparable total magnitude: NGC 4616 and NGC 4603D, both at an angular separation of about 7 arcmin (see Fig. 3 [Plate 89]). Only NGC 4616 has a redshift similar to NGC 4622: 4586 vs 4367 km s^{-1} (de Vaucouleurs *et al.* 1991, hereafter referred to as RC3); it is clearly a possible suspect for the perturbing companion. However, our prime suspect is a smaller galaxy of unknown redshift only 1'.85 to the east (see the object labeled *C*? in Fig. 3). Our reasons for suspecting this galaxy to be the perturber are discussed in Sec. 7.

4. GEOMETRIC AND PHOTOMETRIC PARAMETERS

The inclination and line of nodes position angle of NGC 4622 are important for the interpretation of its structure. The photometric values of these parameters were derived by fitting ellipses to the isophotes in all three filters. In the range $3'' < a < 16''$, isophote shapes are almost exactly round. In the outer regions, the axis ratio and position angle are consistent among the three filters only near the radius (50".8) of the standard isophote where $\mu_B = 25.0$ mag arcsec^{-2}. The resulting orientation parameters are given in Table 1. If the galaxy is intrinsically circular near the standard isophote,

[2] IRAF is distributed by National Optical Astronomy Observatories, which is operated by the Association of Universities for Research in Astronomy, Inc. (AURA), under cooperative agreement with the National Science Foundation.

TABLE 1. Basic parameters.

Parameter	Value
$\log D_{25}(0'.1)$	1.229
$\log R_{25}$	0.060
θ_{25}	174°
B_T	13.37
$\log A_e(0'.1)$	0.88
$(B-V)_T$	0.96
$(V-I)_T$	1.28
$B(0)_c$ (mag arcsec^{-2})	21.79
$\log r_e^{\rm I}$ (kpc)	0.23
$\log r_e^{\rm II}$ (kpc)	0.75
μ_e^c(I) (mag arcsec^{-2})	22.02
μ_e^c(II) (mag arcsec^{-2})	23.61
$\Delta m_1(B)$	1.17

then the axis ratio of $R_{25}^{-1} = 0.87$ corresponds to an inclination of about 30°. Owing to the obvious interaction, this assumption may not be valid and should be confirmed kinematically.

A few standard photometric parameters are also compiled in Table 1. The integrated magnitude, $B_{\rm T}$, and colors, $(B-V)_{\rm T}$ and $(V-I)_{\rm T}$, were computed by integrating the flux in circular apertures after all field stars were removed. The removal of these stars was an important task not only for this purpose, but also for the analysis discussed in Sec. 6. The technique we used, especially for the bright star only 10″ northeast of the center, is discussed by Crocker & Buta (1992). Both $B-V$ and $V-I$ reached an asymptote within the CCD field, but for the magnitude, we fitted an RC3 standard growth curve to account for a small amount of light outside the field. Using the redshift as a distance indicator and a Hubble constant of 100 km s^{-1} Mpc^{-1} (Buta & de Vaucouleurs 1983), we estimate a distance of 42 Mpc, which gives an absolute magnitude of $M_{\rm T}^0(B) = -20.4$. This high luminosity seems consistent with the sharpness of the spiral arms, typical of van den Bergh luminosity class I galaxies.

The shape of the inner ring of NGC 4622 was mapped in all three filters using a cursor on a television display. The following mean parameters are based on ellipse fits to 54–58 visually estimated points: apparent diameter 46″.9 ± 0″.1, apparent axis ratio 0.90 ± 0.01, and major axis position angle 86° ± 2°. The angular diameter corresponds to 9.5 kpc at a distance of 42 Mpc. Inner rings in SA galaxies of similar Hubble stage to NGC 4622 tend not to be this large on average (Buta & de Vaucouleurs 1982). The ellipse fits also showed that the center of the ring is displaced 2″.3 west, 1″.3 south of the nucleus, corresponding to a total linear displacement of about 550 pc. This amounts to 11.5% of the major axis radius of the ring. The displacement of the nucleus is not along the projected major axis of the ring, but along a position angle of 61° ± 2°.

The shapes of the spiral arms were also mapped visually. The leading arm was defined using a 1θ *B*-band Fourier image (see Sec. 6) and found, within errors, to be logarithmic about the nucleus over the radius range $14''.5 \lesssim r \lesssim 21''.5$, with a pitch angle of 3°.8 [Fig. 4(a)]. This was found to be true only in projection; if the galaxy is inclined 30°, around the position angle 174°, then the leading arm is definitely not logarithmic and is not otherwise characterized by a monotonically increasing or decreasing phase with increasing radius. The two outer arms were mapped using the *V*-band image and neither was found to be as logarithmic in projection, within the errors, as the leading arm. Approximate logarithmic fits gave pitch angles of 7° for the east arm [Fig. 4(b)] and 8° for the west arm [Fig. 4(c)].The east arm appears to be slightly better represented by a linear variation of the phase angle with increasing radius, with pitch angle varying as arccot $(4.1/r)$ in the range $25'' \lesssim r \lesssim 45''$ [Fig. 4(d)]. Just as for the leading arm, allowing for the photometric orientation parameters does not improve the simple mathematical representation of the two outer arms. These findings imply that the galaxy may be almost exactly face on.

5. COLORS OF FEATURES

The fits in Figs. 4(a), 4(c), and 4(d), in addition to the ellipse fit to the inner ring, were used to make the schematic in Fig. 2. In Fig. 5, we present a more quantitive illustration of the color distribution in the main features in NGC 4622 using a binning technique similar to that employed by Schombert *et al.* (1990). To make the plots in Fig. 5, we integrated the intensity arrays within a 3″ circular aperture positioned along the features using the coordinate mappings discussed in Sec. 4. For the outer arms and ring, we used the visual point mappings from Fig. 4, while for the leading arm we used the logarithmic spiral fit from position angle 90° to 380° to define a set of coordinates spaced every 10°. The colors were divided into four intervals of $B-V$, and all points within each interval are plotted on the same schematic as in Fig. 2.

The leading arm is found entirely within the reddest color range illustrated. In the position angle range $90° \leqslant \theta \leqslant 360°$, corresponding to the part of the leading arm which is confined within the inner ring, the average colors are $\langle B-V \rangle = 1.04$ and $\langle V-I \rangle = 1.29$, and the average surface brightness within the 3″ apertures is $\langle \mu_B \rangle = 22.7$ mag arcsec^{-2}. To quantify the lack of color contrast between the leading arm and its surroundings further, we integrated the intensity arrays in two identical logarithmic patterns offset by ± 3″ in radius from the leading arm. This gives colors of the local underlying background. In the position angle range $90° \leqslant \theta \leqslant 360°$, the regions immediately inside the leading arm have colors $\langle B-V \rangle = 1.03$, $\langle V-I \rangle = 1.32$, while in the position angle range $90° \leqslant \theta \leqslant 270°$, the regions immediately outside the leading arm have $\langle B-V \rangle = 1.03$, $\langle V-I \rangle = 1.30$. The color contrast is, therefore, negligible.

Figure 6 shows a color–color diagram for all of the points illustrated in Fig. 5. For this plot, the $B-V$ colors were corrected for galactic extinction, inclination, and redshift, using RC3 procedures. For $V-I$, we used information from Rieke & Lebofsky (1985) and Coleman *et al.* (1980), in

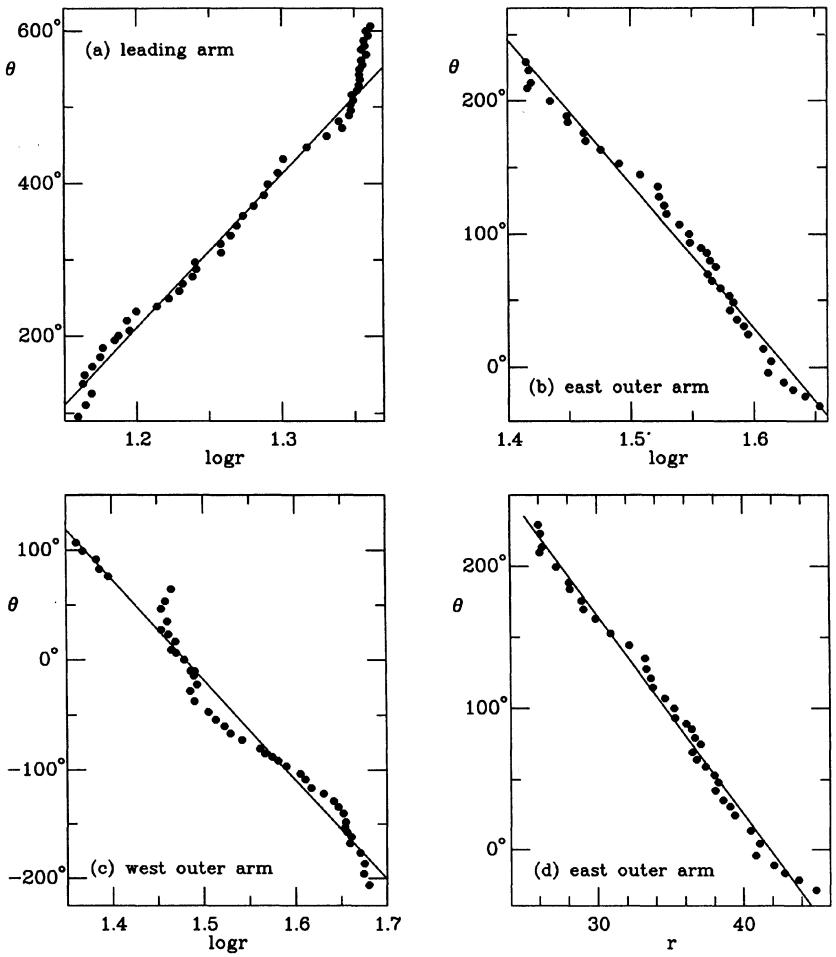

FIG. 4. Dependence of the phase (θ, measured east with respect to north) on radius (r) in arcseconds for the leading arm and the two outer trailing arms of NGC 4622. These are based on visual judgments of the shapes from images on a television display. The east and west outer arms are identified in Fig. 2.

addition to RC3 data. Also displayed in Fig. 6 are the corrected photoelectric total colors for a sample of 36 ringed galaxies in the type range $S0^+$ to Sbc (Buta & Crocker 1992). In a $(U-B, B-V)$ color–color plot, these galaxies follow the standard galaxy sequence closely (see, e.g., Larson & Tinsley 1978), suggesting that they should be a good comparison sample. The colors of the ring, leading arm, and outer arms of NGC 4622 follow closely the color–color relation of normal galaxies.

6. DECOMPOSITION OF THE LUMINOSITY DISTRIBUTION

In the direct images, the leading arm in NGC 4622 is apparent but has a low contrast compared to the two outer arms. To improve the contrast of the feature, we have used two methods to remove the high amount of background light of the central disk. In the first method, we use a standard bulge/disk decomposition which involves conventional fitting functions, and then we subtract the combined model from the total intensity array. In the second method, we derive the seven lowest-order Fourier terms ($n = 0$–6) in the expansion of the luminosity distribution, and use these to create images of the main components. This turns out to be a powerful way of illustrating the structure of the leading arm, and makes no assumptions about the form of the axisymmetric background.

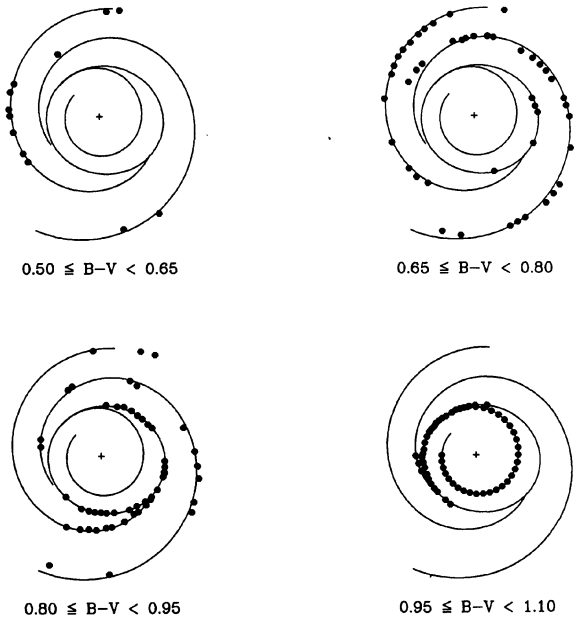

FIG. 5. Quantitative distribution of colors of the main features in NGC 4622 in four ranges of $B-V$, superposed on the same schematic as in Fig. 2 (see text). The plus symbol indicates the nucleus.

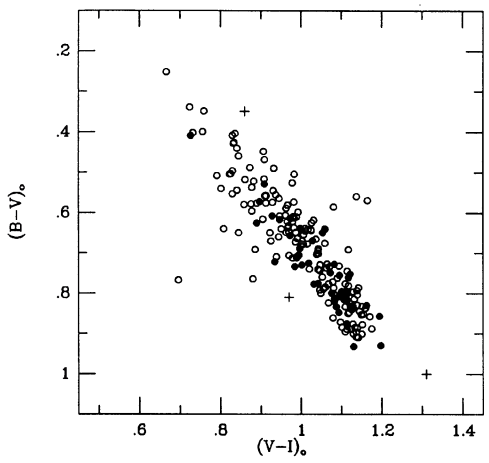

FIG. 6. Color–color plot for the arms and ring in NGC 4622, based on the points displayed in Fig. 5 (see text). The open circles represent these points, while the filled circles represent the integrated colors of a sample of normal ringed galaxies in the type range S0$^+$ to Sbc. The plus symbols refer to the colors of the three main components (bulge, disk, and net arms) from Table 3.

6.1 Standard Profile Decomposition

The technique of standard profile decomposition has been widely applied to galaxies of all types (see review by Okamura 1988; Knapen & van der Kruit 1991). For the bulge component, we use an $r^{1/4}$ fitting function,

$$\mu^{\rm I} = \mu_e^{\rm I} + 8.3268[(r/r_e^{\rm I})^{1/4} - 1],$$

while for the disk we use an exponential fitting function in log units,

$$\mu^{\rm II} = \mu_e^{\rm II} + 1.8225[(r/r_e^{\rm II}) - 1].$$

The four parameters to be derived are the effective surface brightnesses, $\mu_e^{\rm I}$ and $\mu_e^{\rm II}$, and the effective radii, $r_e^{\rm I}$ and $r_e^{\rm II}$. The superscripts follow the notation used by Simien & de Vaucouleurs (1986). We used nonlinear least-squares routines from Press *et al.* (1988) to fit the above functions and solve for these parameters.

Because NGC 4622 is nearly face on, we used the following combined profile for the fit in each passband. For the bulge-dominated region, $r < 12''$, we used a circularly averaged profile since this characterizes isophote shapes in this region. For the disk-dominated region, $r > 58''$, we used an elliptically averaged profile within annuli having an axis ratio of 0.87 and a position angle of 174°, consistent with isophote shapes at the standard isophote level. Between these two zones the spiral structure is prominent, and the surface brightnesses cannot be used in the fits.

In the actual fits, we tried to account for the effects of seeing in the central few arcseconds using a table of convolution corrections for the $r^{1/4}$ law (see discussion in Capaccioli & de Vaucouleurs 1983). The corrections were applied iteratively as described by Tsikoudi (1977), and assume that the bulge dominates within at least the inner 8″. The corrections depend on σ^*, the Gaussian width of the seeing profile, which, following Tsikoudi (1977), we approximated by σ_1^*, the width of the first and most important gaussian component. The adopted values were $\sigma_1^* = 0.88$, 0.87, and 0.83 arcsec for the *B*, *V*, and *I* filters, respectively.

The results of the fits are displayed in Fig. 7 and summarized in Table 2, which also gives the fractional luminosity, *k*, of each component. For both components the effective radius increases from *B* to *I*, implying color gradients in the sense that each component gets *redder* with increasing radius. However, the formal errors on the effective radii are such that we cannot be certain that the gradients are real; they may be artifacts of the fitting procedure, since the decomposition assumes that both components coexist at all radii. The gradients could also be caused by small sky subtraction errors. A by-product of our decomposition is that it allows us to compare NGC 4622 with other galaxies which have been similarly analyzed. Our best-fitting *B*-band values for the effective radii and surface brightnesses of the bulge and disk components lie well within the range found for a large sample of galaxies by Simien & de Vaucouleurs (1986). Table 1 gives the values of the corrected disk central surface brightness, $B(0)_c$, the fractional contribution of the bulge in magnitudes, $\Delta m_1(B)$, linear values of the effective radii based on a distance of 42 Mpc, and corrected effective surface brightnesses, all as defined by Simien & de Vaucouleurs (1986). Table 3 provides integrated magnitudes and colors of the bulge and disk components based on the model parameters, both uncorrected and corrected for galactic extinction, inclination, and redshift. These colors are plotted as plus symbols in Fig. 6, which shows that the component colors scatter around the normal galaxy relation in a manner which may reflect more the uncertainties in the decomposition model than any intrinsic departures. The corrected *total* colors of NGC 4622 (last line in Table 3) lie completely within the distribution of the comparison galaxies.

With model bulge and disk parameters, we can now subtract the sum of these components from the images. For this purpose, we assumed apparent flattenings of 1.0 for the

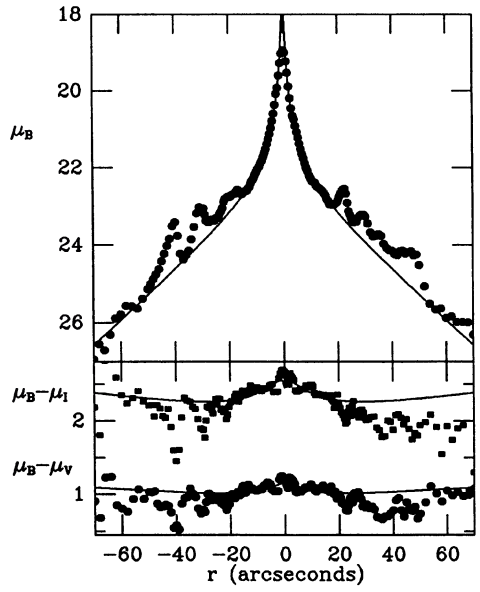

FIG. 7. Results of standard bulge/disk decomposition superposed on a *B* band major axis profile (position angle = 174°) and the corresponding color index profiles. Units are mag arcsec^{-2}. Positive radii extend southward, while negative radii extend northward.

TABLE 2. Results of profile decompositions.

Parameter	*B*	*V*	*I*
μ_e^I (mag arcsec^{-2})	22.56	21.43	20.11
r_e^I (arcseconds)	8.4	8.5	9.2
μ_e^{II} (mag arcsec^{-2})	24.00	23.10	22.00
r_e^{II} (arcseconds)	27.6	28.7	29.3
k_I	0.34	0.41	0.49
k_{II}	0.45	0.45	0.40
k_{III}	0.21	0.14	0.11

bulge and 0.87 for the disk. The residual is the spiral component, whose fraction is given by k_{III} in Table 2. The subtraction was performed in all three filters, and the results for *B* and *I* are displayed in the lower left and right panels, respectively, of Fig. 1. Removal of the dominant background components (which account for 79% and 89%, respectively, of the total *B*- and *I*-band luminosities; see Table 2) dramatically enhances the leading arm as a smooth, curved feature which appears to begin near the position of the bright foreground star close northeast of the nucleus. After winding some 360°, it appears to blend into the east half of the inner ring, which is also the red half of the ring (see color index map, Fig. 1). The leading arm also appears not to extend into the bulge-dominated region.

6.2 Fourier Decomposition

Fourier decomposition has not been widely used in studies of nonbarred spiral galaxies but is a potentially powerful way of probing the structure of NGC 4622 (see, e.g., Considère & Athanassoula 1988). We have decomposed NGC 4622 into its first seven components by computing averages of $I(r,\theta) \times \cos n\theta$, and $I(r,\theta)\sin n\theta$ as a function of radius, *r*, where I refers to sky-subtracted and sky-normalized *intensities* (any filter), θ is the position angle in the galaxy plane, and *n* is an integer. Calculation of these averages at all radii allows us to construct images in any individual component or combination of components. For example, an $n = 1$ image will tend to emphasize any large-scale asymmetries, such as the leading arm and the lopsided part of the outer arms, while the $n = 2$ image will tend to emphasize any large-scale bisymmetries, such as the outer arms or a bar or oval, if present. Since the galaxy appears to be nearly face on, for the purposes of the decomposition, we have used circular averages (as opposed to elliptical averages). Even if the galaxy is actually inclined up to 30°, our analysis is not seriously compromised with circular averages because we are interested in simply characterizing the apparent morphology. Reliable estimates of the amplitudes and phases of any nonaxisymmetric component would, of course, require taking into account the inclination. We are interested in characterizing the stellar distribution in the galaxy, therefore, we illustrate our main Fourier decomposition results in the *I* band.

TABLE 3. Colors and magnitudes of components.

Component	*B*	*V*	*I*	$B-V$	$V-I$	$M_T^o(B)$	$(B-V)_o$	$(V-I)_o$
Bulge	14.55	13.38	11.89	1.18	1.48	−19.2	1.00	1.31
Disk	14.25	13.27	12.12	0.98	1.15	−19.5	0.81	0.97
Arms	15.08	14.56	13.52	0.52	1.04	−18.7	0.35	0.86
Total	13.38	12.41	11.12	0.98	1.28	−20.4	0.80	1.11

The axisymmetric, or $n = 0$, part is illustrated in the upper-right panel of Fig. 8 [Plate 90], which shows a prominent ring corresponding to the inner ring and several fainter rings associated with the outer arms. The largest nonaxisymmetric amplitudes are provided by the $n = 1$ and 2 components, which are the only ones we illustrate (see the lower-left and lower-right panels of Fig. 8, respectively). The $n = 1$ image dramatically illustrates the leading arm, which again appears to trace out more than 360°, and may include a substantial portion of the inner ring. Structure beyond the leading arm reflects mostly the asymmetry associated with the two outer arms. The $n = 2$ component is dominated by the two outer arms, but is interesting in the lack of significant amplitude within the inner ring. These demonstrate that most of the structure of NGC 4622 is adequately represented by the lowest-order terms. The upper-left panel of Fig. 8 shows a reconstructed *I*-band image (in units of mag arcsec^{-2}) based on $n = 0$–6 Fourier amplitudes.

Figures 9(a) and 9(b) show the $n = 1$ and 2 amplitudes and phases to a radius of 70″ (the limit imposed by the CCD field), for all three filters. The radii are normalized to the standard isophote, $r_{25} = 50''.8$ (Table 1). The amplitudes are normalized to the average intensity, I_0, at each radius. The most obvious part of the leading arm lies in the range $0.29 \leqslant r/r_{25} \leqslant 0.42$ and reaches a maximum relative amplitude in *I*-band light of $I_1/I_0 = 0.144$ at $r/r_{25} = 0.354$. The dependence of the amplitude on wavelength is smaller than in the outer disk, again demonstrating the arm's rather red color. The increase of the phase θ_1 with increasing radius of the leading arm is readily apparent. The phase of the $n = 2$ component for $r/r_{25} \gtrsim 1$ scatters around a position angle of 175°, consistent with the major axis position angle derived from ellipse fits.

We now focus on a few specific aspects of the Fourier images needed for the discussion in the next section. In Fig. 10, we illustrate an isophote map of the $n = 1$ image displayed in Fig. 8. The leading arm stands out as a continuous feature, but more importantly, there are two definite minima along the arm (labeled A and C in Fig. 10). The principal maximum (labeled B) is the prominent part of the leading arm, which, as mentioned above, corresponds to the small peak in relative $n = 1$ amplitude at $r/r_{25} = 0.354$ in Fig. 9(a). The azimuthal surface brightness profiles associated with this peak are illustrated in Fig. 11(a); there is only a small shift in θ_1 with filter at this radius. The second principal maximum, labeled *D* in Fig. 10, shows a much larger phase shift, $\Delta\theta_1 \approx 40°$, and is associated with a peak in the relative $n = 1$ amplitude at $r/r_{25} = 0.45$. This shift, which is illustrated clearly with the corresponding azimuthal profiles in Fig. 11(b), has interesting implications for the nature of the ring. For comparison, Fig. 11(c) shows an azimuthal profile at $r/r_{25} = 0.67$, which corresponds to the first major peak in the $n = 2$ relative amplitude shown in Fig. 9(b). No shift in phase θ_2 with filter is associated with this peak. Finally, Fig. 11(d) shows the variation in $B - I$ color with phase around the inner ring itself (not at a fixed radius). A very large amplitude of 0.45 mag is revealed.

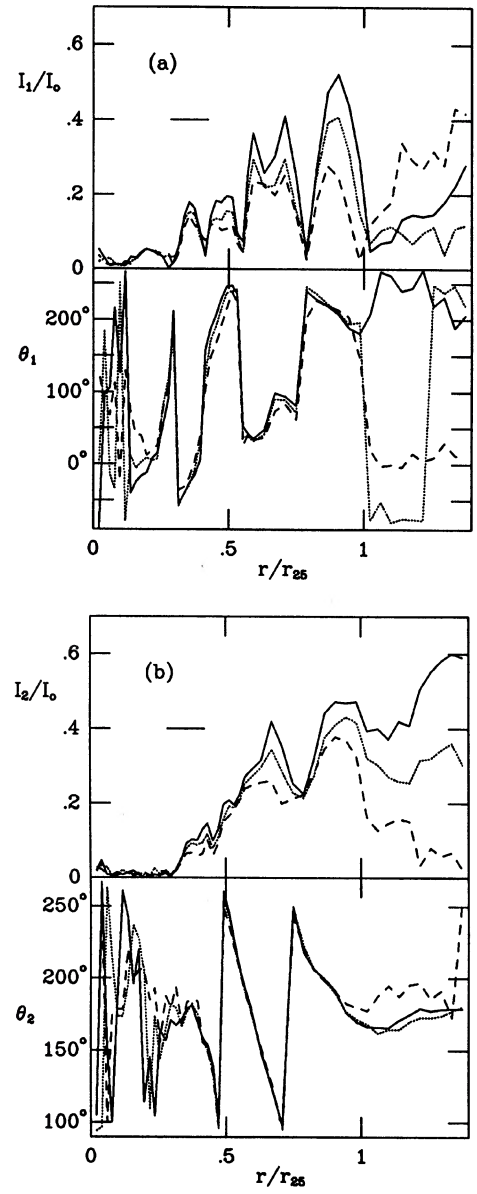

FIG. 9. Dependence of relative Fourier amplitudes and phases (measured eastward with respect to north) on radius normalized to the radius of the standard isophote: (a) $n = 1$ term and (b) $n = 2$ term. In both plots, the solid lines refer to the *B* band, the dotted lines to the *V* band, and the dashed line to the *I* band. The horizontal line in each case refers to the region where the leading arm is prominent inside the inner ring.

7. DISCUSSION

The observations presented here have confirmed the reality of the leading arm and ruled out the possibility that it is an artifact of an unusual dust pattern. These observations have also quantified some of the feature's characteristics. The effects of a circularly orbiting retrograde companion on a disk system were first demonstrated analytically by Athanassoula (1978). It was found that this circumstance emphasizes a strong one-armed leading spiral component in both the stars and gas. NI86 and T89 confirmed the analytic results using *n*-body simulations for a companion on an unbound orbit. The self-gravitating simulations of T89 made the interesting finding that tidally generated leading arms are favored only when the mass of the halo component is greater than or approximately equal to that of the disk component. Low-mass haloes favored trailing spiral patterns which are strengthened by Toomre's (1981) local swing amplification mechanism in the disk. The proximity of the leading arm to the bulge region of NGC 4622 is consistent with the high halo requirement of T89.

In spite of extensive searches, leading arms appear to be very rare. On the basis of the argument that retrograde companions should be as common as direct ones, and that encounter orientations are random, T89 suggested that perhaps 25% of all spirals with major companions should have a leading arm generated via a strong retrograde perturbation. Recently, Keel (1991) confirmed that direct and retrograde companions are equally common in a sample of Karachentsev pairs. However, the observational evidence (T89; Iye & Sugai 1991) favors a much smaller fraction of leading arms than expected, indicating either that most galaxies may have a halo mass less than or approximately equal to their disk mass, or, alternatively, that there are tight constraints on companion orbits or masses. If the former is correct, it would, of course, have important implications for the general dark matter problem, since it is not consistent with the inferences from other indications (see discussion in Valtonen & Byrd 1990).

It is interesting that both the NI86 and T89 simulations generate a leading arm which closes into an off-centered ring much like the ring seen in NGC 4622. On the basis of these models, we interpret the leading arm and ring as a set of $m = 1$ dispersion orbits. Here, we refer only to the portion of the disk inside $0.5r_{25}$ where the two outer trailing arms are not strong. For each dispersion orbit, $\Omega_p = \Omega - \kappa/m$, where Ω is the orbital angular rate of the disk material, κ is the epicyclic frequency, m is the multiplicity of the density peaks of the dispersion orbit, and Ω_p is the pattern speed. In the case of unbound passages, a +1:1 resonance can occur with Ω_p nearly equal to the angular rate of the companion at closest approach (Athanassoula 1992). For an $m = 1$ dispersion orbit, under the reasonable assumption that the circular orbital velocity, V, is constant with radius r, and that self-gravity is unimportant, the precession angular rate would be $\Omega - \kappa = (1 - \sqrt{2})V/r = -0.414V/r$. Note that this number is negative at all radii: It corresponds to a motion opposite the general direction of the rotation, which we infer from the outer arms to be counterclockwise in our illustrations. Since $\Omega - \kappa$ is larger at smaller radii, we expect an ensemble of the $m = 1$ dispersion orbits to form a leading arm, winding outward against the direction of the disk rotation (compare with the trailing kinematic density waves illustrated by Kalnajs 1973). The strongest portion of the leading arm may be disk material that formed an $m = 1$ ILR with the angular rate of motion of a companion at closest approach.

This also implies that there will be a difference between the phase, θ_1, of the $n = 1$, *I*- and *B*-band peaks in the region where gas is abundant that is closely analogous to that expected for two-armed density wave patterns (e.g., Roberts *et al.* 1975; Schweizer 1976). At a given radius, we expect a concentration first of stars and gas (*I*-band enhancement) as

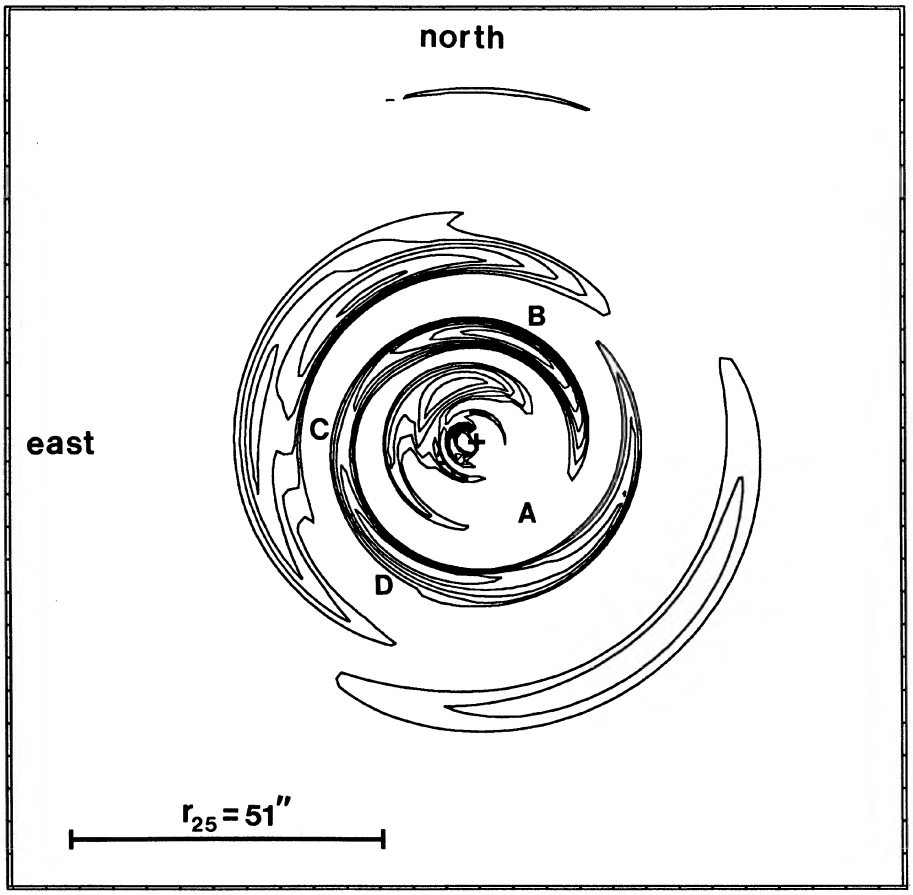

FIG. 10. Contour map of $n = 1$ surface brightness in the I band. The labels A–D refer to different parts of the leading arm (see text). The lowest contour is for 10 ADU, and each successive contour is spaced by 10 ADU.

the disk material enters the $m = 1$ density wave. Then at a larger θ, there would be a B-band enhancement due to the time lag between gas compression, and star formation and evolution. These stars will appear predominantly blue via the extremely luminous, hot, short-lived, main-sequence stars.

The main part of the leading arm (feature B in Fig. 10) has very few blue stars and probably little gas in the region of the disk where it occurs. There is also little shift in θ_1 in this region from B to I. However, we found that feature D in Fig. 10, which is part of the inner ring, displays a 39° phase shift whose sense is such that θ_1 *increases* from I to B [see Fig. 9(a)]. We indicate the phase of the $n = 1$ component by vertical bars in the azimuthal plots in Fig. 11(b), which are for the radius where the phase shift is largest, and note how the V-band peak is placed nicely between those for B and I. The difference is significant, and we suggest that it is an indication of the compression, star formation, and dispersion time lag mentioned above, in the expected sense of a backwardly precessing $m = 1$ dispersion orbit.

What time lag, in years, does this difference in position angle indicate? Based on the galaxy's luminosity and type, we can reasonably guess the maximum rotation velocity to be ≈ 250 km s^{-1}. The I-band intensity variation at the average radius (4.65 kpc) of the inner ring is only 12% over the circular average, so the epicyclic velocity variations are small compared to the orbital velocity. The angular speed of the compressed gas relative to the $m = 1$ density peak is the difference of the orbital angular rate minus the pattern precession angular rate, or $\Omega - \Omega_p = 1.4\, V/r$. This difference divided by the observed 0.68 rad difference in position angle equals the time lag for star formation. Using the values for the various quantities given above, we find a time lag of order 10^7 yr, which is not unreasonable.

There are other reasons why the inner ring is not likely to be the result of a resonance with the pattern speed of a two-armed density wave associated with the outer trailing arms, as may be the case for some other rings (e.g., NGC 5364, Lin 1971). Indeed, the outer arms show a significant degree of lop-sidedness, and the phase θ_2 of the $n = 2$ component displays a linear (position angle, radius)-relation characteristic of tidal "material" arms created by the close passage of a small companion (see, e.g., Howard & Byrd 1990 for a discussion of such arms in M51, the prototypical tidally perturbed galaxy). Our images also reveal no evidence for even a weak oval in the inner region. One can see in Fig. 9(b) that the variation of θ_2 with radius is mostly independent of filter, which is what we expect for short-term tidal material arms where the particles stay in the arms as they move with roughly the orbital angular rate. Note also that the difference between the angular rates of the pattern maximum and the orbital motion is smaller, $\Omega - \Omega_p = 0.7V/r$, for trailing twofold dispersion orbits for a $V =$ constant disk. Thus, a phase shift, similar to that found in the inner ring, would be more difficult to detect in the outer arms.

The models in T89 were not designed specifically for

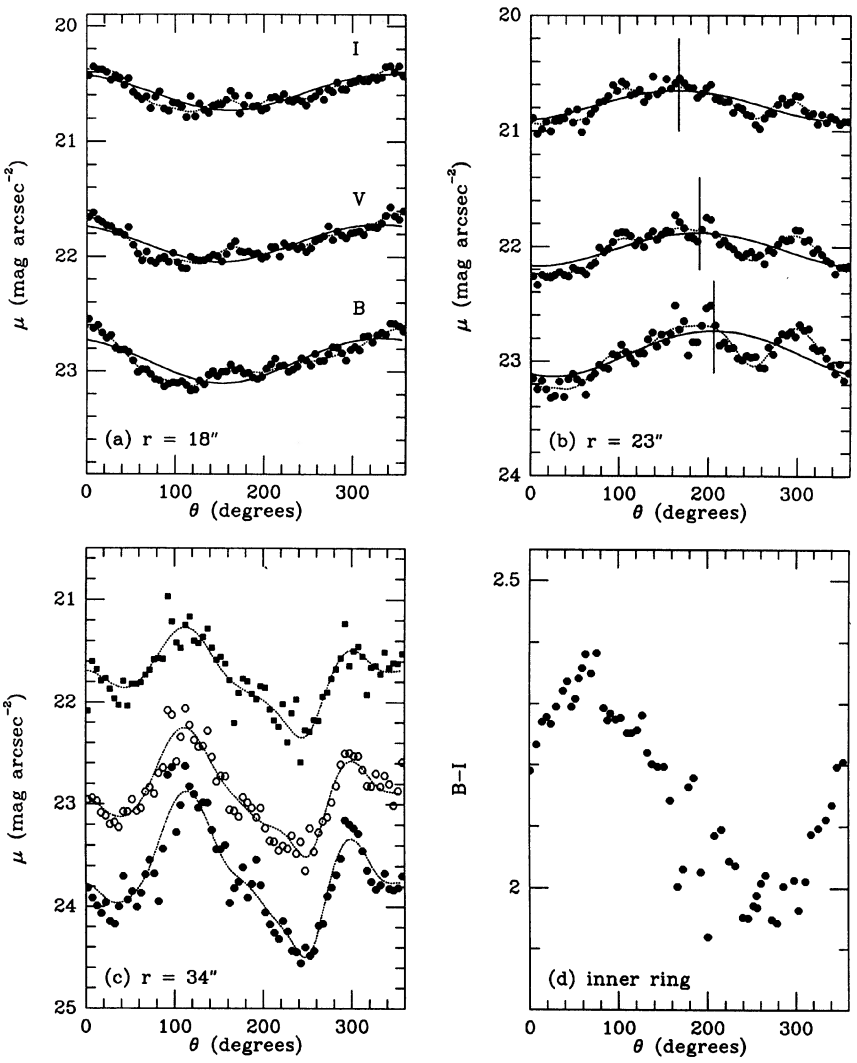

FIG. 11. Azimuthal *BVI* surface brightness profiles for three radii: (a) The prominent part of the leading arm inside the inner ring (feature B in Fig. 10); (b) the average radius of the inner ring (feature D in Fig. 10; vertical bars denote phase of the $n = 1$ Fourier component); and (c) a radius in the region of the two outer arms. For (a)–(c), the filters are I (top profile), V (middle profile), and B (bottom profile). Different symbols had to be used in (c) to prevent confusion. Solid curves in (a) and (b) refer to $n = 0 + 1$ components alone, while the dotted curves in (a)–(c) show the full $n = 0$–6 sums. Panel (d) displays an azimuthal color index profile around the off-centered inner ring, highlighting the large amplitude color variation around this feature.

NGC 4622 but were for a general study of leading and trailing arm formation. Furthermore, those simulations did not show the outer trailing arms coexisting with a leading arm as seen in NGC 4622. We are currently carrying out a more extensive simulation study in an attempt to create the spiral arms, both leading and trailing (Freeman *et al.* 1992). In this regard, it is interesting that Struck-Marcell (1990) has proposed a variant on our encounter hypothesis to explain the appearance of NGC 4622: He mentions this galaxy as a possible example of the creation of a spiral or thick braided ring by a slightly off-center, high-velocity, highly tilted collision with a small galaxy [see his Figs. 2(b), 2(c), and 4(b)]. The ring could then be related to those seen in collisional "ring" galaxies. Unfortunately, the SRC-J photograph of NGC 4622 cited by Struck-Marcell (from the Arp & Madore 1987 catalog) shows only the outer trailing arms with the nucleus overwhelming the leading arm and ring. Struck-Marcell's simulation has a thick braided ring with loops resembling the outer trailing arms and has no leading arm like Byrd saw in the remarkably clear "discovery" photograph (see discussion in Sec. 3).

In our simulations, we are able to reproduce the leading arm and pair of trailing arms of NGC 4622 fairly successfully. Coincidentally, we have found that a very close, plunging passage of a small mass companion, like those being considered by Struck-Marcell, seems to produce the best match rather than the exterior retrograde passages studied by T89. However, our orbital parameters are different, with the passage being in the disk plane and retrograde rather than being highly inclined as in Struck-Marcell's studies. Since we find that the companion must be low mass (as does Struck-Marcell), the small galaxy 1'.85 east of NGC 4622 is a viable suspect for the creation of the leading arm and worthy of future observation.

8. CONCLUSIONS

The southern galaxy NGC 4622 presents one of the most convincing cases of a leading arm in a tidally disturbed spiral. It is not the first galaxy where a leading arm has been suggested to exist (see, e.g., Simien *et al.* 1978; Kormendy & Norman 1979; Pasha 1982, for some recent considerations). However, the other cases suggested thus far involve either purely one-armed spirals (e.g., NGC 4378) with the near edge being unknown, or are so highly inclined (e.g., M31)

that the arm structure is not clear enough to make a definitive case. In addition, some suggested cases, like NGC 5395 (Pasha & Smirnov 1982), did not stand up to the test of further observation (e.g., Sharp & Keel 1985). In contrast, NGC 4622 has two extremely important aspects that make for an unambiguous interpretation: (1) a face-on orientation, so that the spiral structure is clear; and (2) the coexistence of both one and two-armed patterns winding in opposite senses. If the inner arm is indeed real and not an artifact of dust absorption, then we have a definitive case of a leading arm spiral, regardless of whether the leading pattern is the inner arm or the two outer arms.

Using *BVI* surface photometry, we have shown that the inner, single arm is real and is not an artifact of an unusual dust distribution within an inner ring. Since the feature has low contrast, we used two independent techniques to enhance its visibility. Both methods have revealed a feature which winds more than 360° beginning $\approx$3 kpc from the center and extending to about 4.4 kpc. The pitch angle of the arm is low, about 3°.8, and it appears to be logarithmic only in projection. The arm has fairly red colors consistent with that of the surrounding background, and is thus largely a stellar-dynamical phenomenon. Other aspects of the galaxy, such as disk/bulge properties and colors, appear to be normal for the type of Sab. The outer arms and part of the inner ring show bluer colors than the inner arm, and appear to include gas dynamics.

The inner ring of NGC 4622 is interesting in that it may be partly made of the leading arm and partly of the trailing arms, which blend into the ring nearly due east and due south of the nucleus. In conjunction with the published models, the appearance suggests that the ring is intimately linked with the $+1{:}1$ resonance with the companion.

NGC 4622 is a strong case for a system with tidally generated spiral structure. The presence of the large difference in the phase of the 1θ Fourier component between the *B* and *I* filters in the inner ring region supports the idea that the inner, single arm is the leading component relative to the disk orbital motion. This galaxy may be the clearest case yet demonstrating this expected density wave color phase shift because the shift is much larger for a one-armed pattern than for a two-armed pattern. In contrast, the outer arms display no significant phase shift from *B* to *I*, suggesting that they are trailing, tidal material arms. It is clear that the kinematics of the system are needed for a definitive interpretation of its structure and history (especially to better establish the inclination), and to this end we plan to obtain imaging Fabry–Perot interferometry. In a separate paper, we discuss our experiments with an improved model of the dynamics.

Note added in proof. We wish to point out that galaxies of the Magellanic Cloud (or SBm) type show "leading spurs" as a characteristic part of the structure [de Vaucouleurs & Freeman, Vistas in Astron., 14, 163 (1972)]. These features are of an entirely different nature than the feature seen in NGC 4622 and reflect more the properties of periodic orbits in a bar potential.

We thank C. Struck-Marcell for helpful comments which improved the presentation of this paper. This work was supported by NSF EPSCoR Grant No. RII 8996152 and by NSF Grant No. AST 9014137 to the University of Alabama.

REFERENCES

Arp, H. C., & Madore, B. F. 1987, A Catalogue of Southern Peculiar Galaxies and Associations, Vol. II: Selected Photographs (Cambridge University Press, Cambridge)
Athanassoula, E. 1978, A&A, 69, 395
Athanassoula, E. 1992, in Morphological and Physical Classification of Galaxies, edited by G. Busarello, M. Capaccioli, and G. Longo (Kluwer, New York), p. 127
Buta, R. 1991, ApJ, 370, 130
Buta, R., & Crocker, D. A. 1992, AJ (in press)
Buta, R., & de Vaucouleurs, G. 1982, ApJS, 48, 219
Buta, R., & de Vaucouleurs, G. 1983, ApJ, 266, 1
Byrd, G. G., Thomasson, M., Donner, K. J., Sundelius, B., Huang, T.-Y., & Valtonen, M. J. 1989, Celest. Mech., 45, 31
Capaccioli, M., & de Vaucouleurs, G. 1983, ApJS, 52, 465
Coleman, G. D., Wu, C.-C., & Weedman, D. W. 1980, ApJS, 43, 393
Considère, S., & Athanassoula, E. 1988, A&A, 76, 365
Crocker, D. A., & Buta, R. 1991, in Astronomical Data Analysis and Software Systems, edited by D. Worrall, C. Biemesderfer, and J. Barnes (ASP, San Francisco) (in press)
de Vaucouleurs, G. 1956, Mem. Comm. Obs., Vol. III, No. 13
de Vaucouleurs, G. 1958, ApJ, 127, 487
de Vaucouleurs, G., de Vaucouleurs, A., Corwin, H., Buta, R., Paturel, G., & Fouquè, P. 1991, Third Reference Catalog of Bright Galaxies (Springer, New York)
Freeman, T., Byrd, G. G., & Howard, S. 1992, BAAS, 23, 1460
Graham, J. A. 1982, PASP, 94, 244
Ioward, S., & Byrd, G. G. 1990, AJ, 99, 1798
Iye, M., & Sugai, H. 1991, ApJ, 374, 112
Kalnajs, A. J. 1973, PASAu, 2, 174
Keel, W. C. 1991, ApJ, 375, L 5
Knapen, J. H., & van der Kruit, P. C. 1991, A&A, 248, 57
Kormendy, J., & Norman, C. 1979, ApJ, 233, 539
Landolt, A. U. 1983, AJ, 88, 439
Larson, R. B., & Tinsley, B. M. 1978, ApJ, 219, 46
Lin, C. C., 1971, Highlights of Astron., 2, 88
Menzies, J. W., Banfield, R. M., & Laing, J. D. 1980, SAAO, Circ. No. 1, 149
Noguchi, M., & Ishibashi, S. 1986, MNRAS, 219, 305
Okamura, S. 1988, PASP, 100, 524
Pasha, I. I. 1982, SvAL, 11, 1
Pasha, I. I., & Smirnov, M. A. 1982, Ap&SS, 86, 215
Press, W. H., Flannery, B. P., Teukolsky, S. A., & Vetterling, W. T. 1988, Numerical Recipes (Cambridge University Press, Cambridge)
Rieke, G. H., & Lebofsky, M. J. 1985, ApJ, 288, 618
Roberts, W. W., Roberts, M. S., & Shu, F. H. 1975, ApJ, 196, 381
Schombert, J. M., Wallin, J. F., & Struck-Marcell, C. 1990, AJ, 99, 497
Schweizer, F. 1976, ApJS, 31, 313
Sharp, N., & Keel, W. C. 1985, AJ, 90, 469
Shu, F.H. 1982, The Physical Universe: An Introduction to Astronomy (University Science Books, Mill Valley)
Simien, F., Athanassoula, E., Pellet, A., Monnet, G., & Courtes, G. 1978, A&A, 67, 73
Simien, F., & de Vaucouleurs, G. 1986, ApJ, 302, 564
Struck-Marcell, C. 1990, AJ, 99, 71
Thomasson, M. 1990, in Paired and Interacting Galaxies, edited by J. W. Sulentic, W. C. Keel, and C. M. Telesco (NASA Conf. Publ. No. 3098), p. 749
Thomasson, M., Donner, K. J., Sundelius, B., Byrd, G. G., Huang, T.-Y., & Valtonen M. J. 1989, A&A, 211, 25
Toomre, A. 1981, in The Structure and Evolution of Normal Galaxies, edited by S. M. Fall and D. Lynden-Bell (Cambridge University Press, Cambridge), p. 111
Tsikoudi, V., 1977, Univ. of Texas Publ. Astronomy, No. 10 (University of Texas Press, Austin)
Valtonen, M. J., & Byrd, G. G. 1990, IEEE Trans. Plasma Sci., PS-18, 38

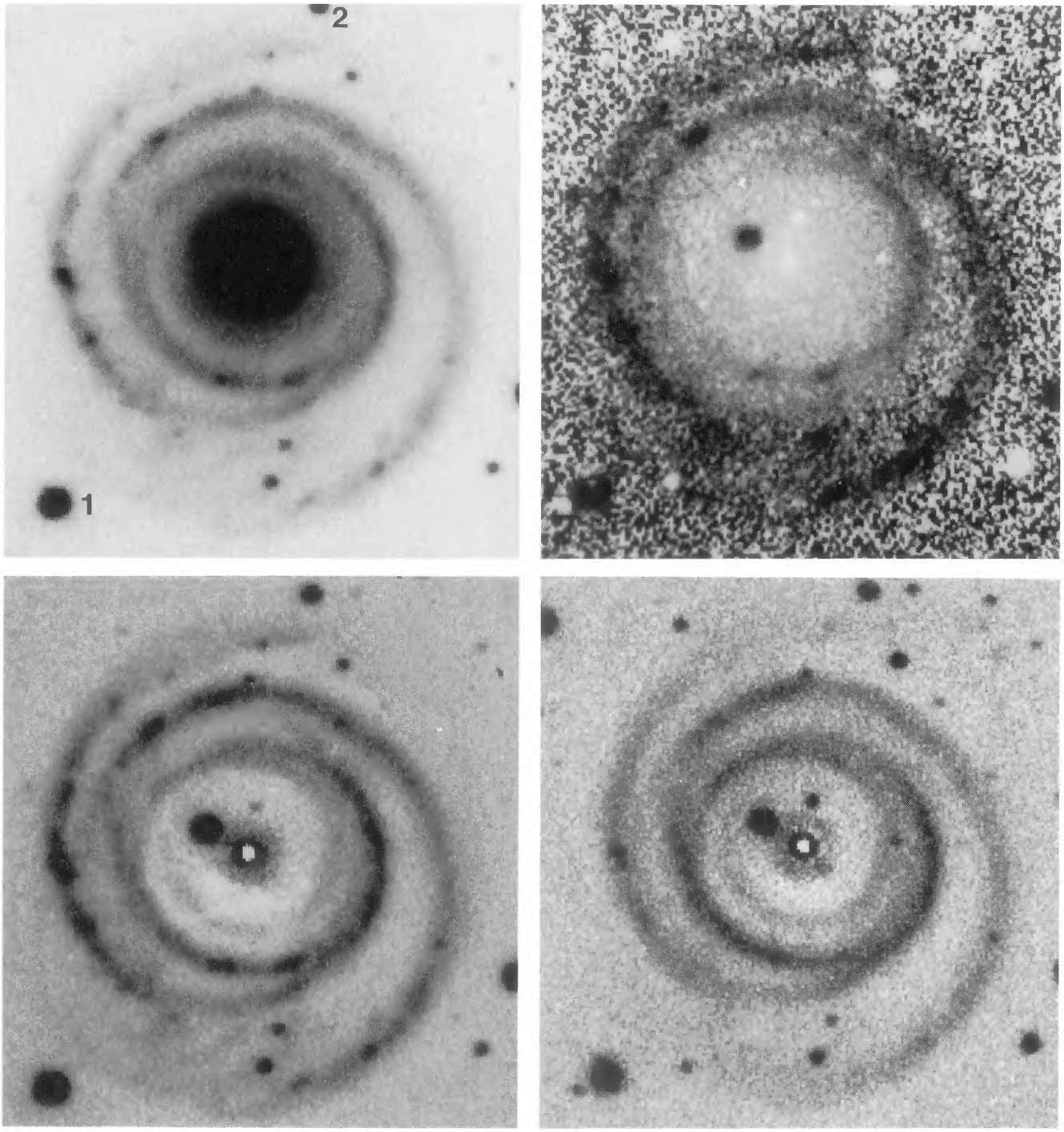

FIG. 1. NGC 4622: (upper left) *B*-band image in intensity units. North is at the top and east is to the left. The two stars labeled 1 and 2 are 106".7 apart and can be used for the scale of all four images as well as those in Fig. 8. (Upper right) $B - I$ color index map. The range displayed is $B - I = 1.75$ (darkest) to 2.75 (lightest). (Lower left) Residual *B* image (intensity units) after subtraction of bulge + disk decomposition model. Note the enhanced appearance of the leading arm, which begins near the bright foreground star close northeast of the center. (Lower right) Same as at lower left, but for the *I* band. [Note: The illustration of this galaxy in Shu (1982) has much better seeing than these images.]

Buta *et al.* (see page 1527)

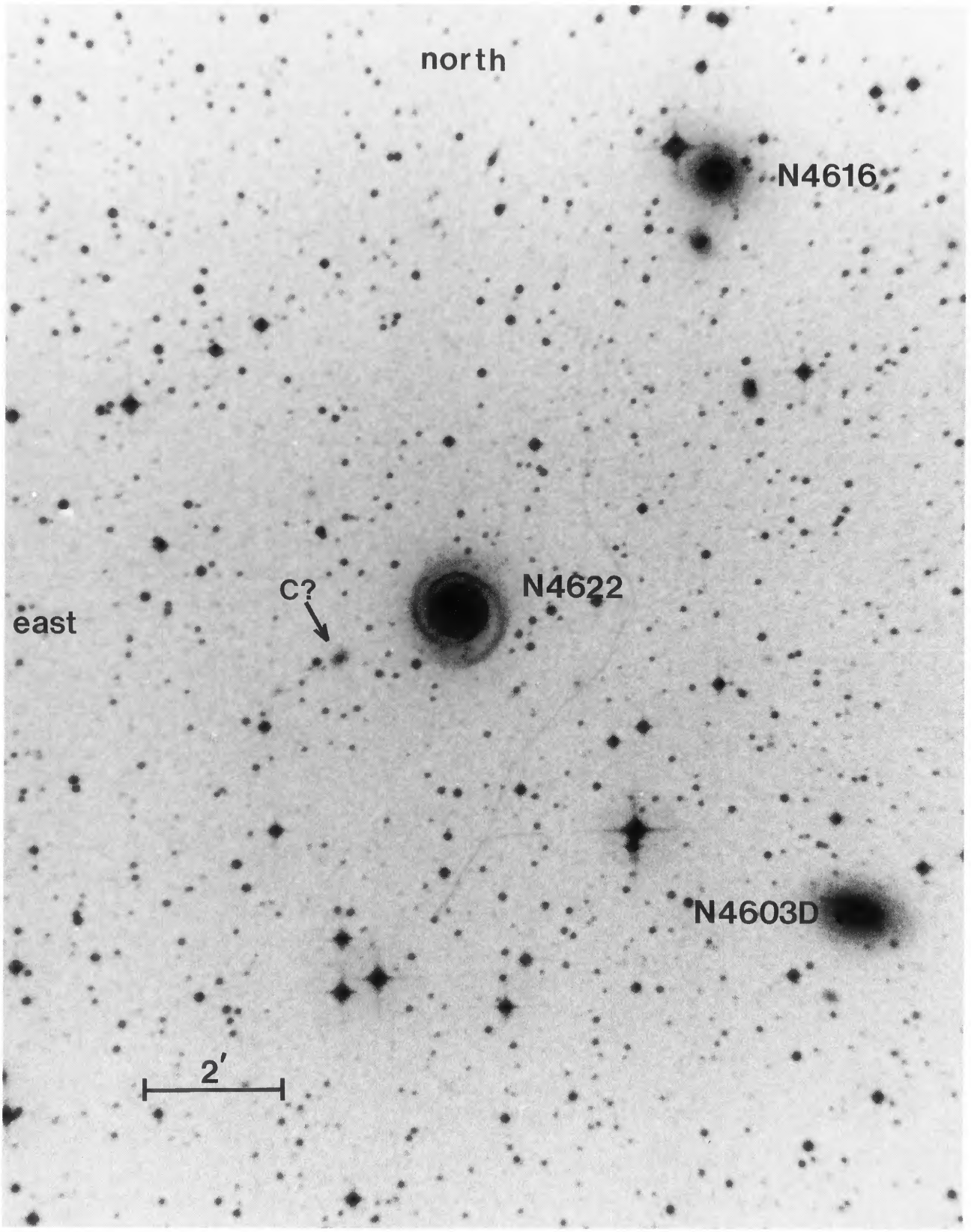

FIG. 3. Reproduction of the field of NGC 4622 from SRC-J copy film 322. Several companions are labeled, and the arrow points to a small galaxy (of unknown redshift and labeled C for companion) which we suspect to be the perturber.

Buta *et al.* (see page 1527)

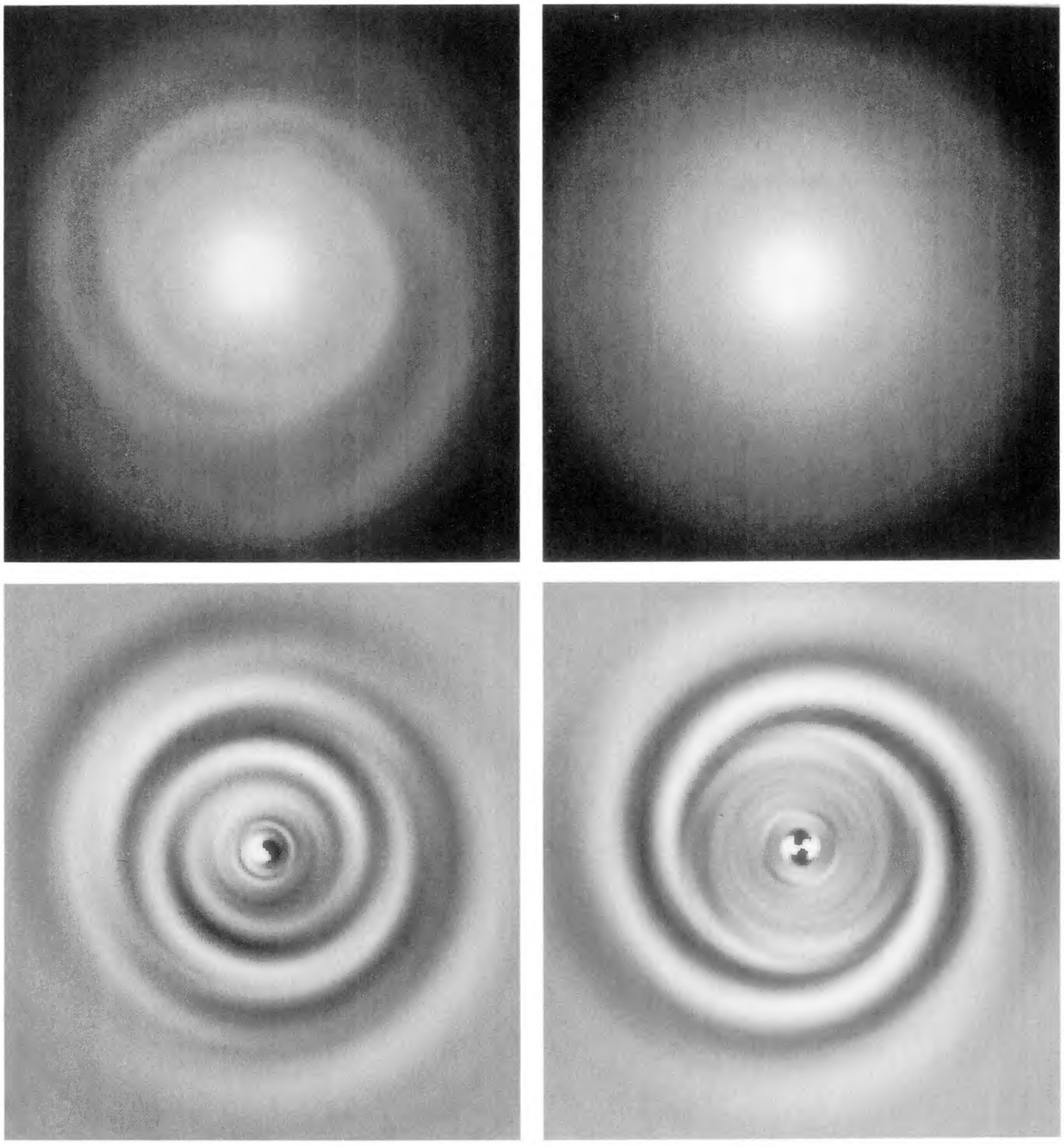

FIG. 8. Fourier decomposition of NGC 4622 (I band): (Upper left) Image reconstructed from the 7 lowest-order terms in the expansion ($n = 0$–6). This image is in units of mag arcsec^{-2}. (Upper right) The $n = 0$ image, also in units of mag arcsec^{-2}. (Lower left) $n = 1$ image, in intensity units. (Lower right) $n = 2$ image, in intensity units. All four of these images are in positive format (as opposed to Fig. 1, where the images are negatives).

Buta *et al.* (see page 1531)

